

Effects of a Shallow Pycnocline and Surface Meltwater on Sea Ice–Ocean Drag and Turbulent Heat Flux

ACHIM RANDELHOFF,* ARILD SUNDFJORD, AND ANGELIKA H. H. RENNER

Norwegian Polar Institute, Tromsø, Norway

(Manuscript received 23 October 2013, in final form 9 May 2014)

ABSTRACT

Comprehensive boundary layer measurements from a drift station on first-year ice in the late summer of 2012 in the Nansen basin, when stable stratification in the upper ocean extended all the way to the surface, are analyzed. Observed quadratic ice–ocean drag coefficients, based on measurements of wind stress, are roughly 3.6×10^{-3} , consistent with neutral-stability Rossby similarity scaling. The turning angles of 32° – 39° between surface velocity and stress are larger than Rossby similarity predicts and obey a different scaling. This can be explained by the shallow pycnocline forcing the Ekman transport into a thin layer and modeled roughly employing a simple first-order correction to Rossby similarity. Turbulent shear stress in the ice–ocean boundary layer is on average 3 times smaller than the estimate based on wind stress, possibly because internal wave drag was significant. This lowers vertical scalar fluxes by 38% compared to a scenario where turbulent stress accounts for the total drag. The authors measure an average upward ocean–ice heat flux of 10 W m^{-2} , which is 50% smaller than predicted by a bulk heat flux parameterization. This reduction is attributed to additional sources of heat and freshwater that alter the ice–ocean interface salt balance. This study shows that a commonly used bulk heat flux parameterization is a special case of a simple downgradient parameterization allowing for a modified interface salt budget. For similar wind forcing, observed ice–ocean fluxes of heat and salt were 40%–100% larger when the ice-relative current approached from a nearby pressure ridge keel than otherwise.

1. Introduction

The drift of sea ice is controlled by its momentum budget, which is determined by the drag exerted by the atmosphere and ocean, atmospheric pressure gradient, sea surface slope, internal ice stresses, and Coriolis force (Leppäranta 2011). This study looks into the details of the stress between sea ice and ocean τ_w . The vertical transport of momentum between the two is carried by a combination of turbulent eddies, internal waves, and form drag (e.g., Steele et al. 1989). Thus, sea ice mediates the momentum input from the atmosphere into the ocean and modifies wind-driven turbulent mixing of momentum, heat, salt, and passive tracers in the upper ocean. The common quadratic drag law (e.g., Leppäranta 2011, chapter 5)

$$\hat{\tau}_w = C_D \exp(i\phi) U_i \mathbf{U}_i \quad (1)$$

expresses the kinematic stress $\hat{\tau}_w = \tau_w / \rho_w$, with ρ_w as the density of seawater, as proportional to the square of the ice velocity relative to the undisturbed ocean \mathbf{U}_i , rotated by a fixed turning angle ϕ arising from the Coriolis force. The proportionality constant C_D is the quadratic drag coefficient. Both stress and velocity are given as complex numbers, where the real and imaginary ($i \equiv \sqrt{-1}$) parts point east and north, respectively. The term U_i denotes the magnitude of \mathbf{U}_i . For modeling applications, both C_D and ϕ are chosen empirically (e.g., Lu et al. 2011). The ice–ocean drag coefficient is, however, determined not only by ice properties like the roughness; it also depends on the turbulent momentum flux across the sea ice–ocean boundary layer (IOBL; McPhee 1979). This momentum flux is described by the Ekman equation (Ekman 1905), which in steady state reads

$$if\mathbf{U}(z) = \partial_z \hat{\tau}(z). \quad (2)$$

The term f is the Coriolis parameter, $\hat{\tau}$ is the turbulent (kinematic) shear stress, \mathbf{U} is the water velocity, and ∂_z

* Additional affiliation: University of Tromsø, Tromsø, Norway.

Corresponding author address: Achim Randelhoff, Norwegian Polar Institute, Fram Centre, 9296 Tromsø, Norway.
E-mail: achim@npolar.no

denotes partial derivation with respect to the vertical coordinate z (pointing upward). Introducing the eddy viscosity K as $\hat{\tau} = K\partial_z \mathbf{U}$, the Ekman equation allows us to encode the turbulent boundary layer in an eddy viscosity profile.

A common conceptual model of the steady-state boundary layer under sea ice consists of a constant stress surface layer and an Ekman spiral-like outer layer (e.g., [Morison and McPhee 2001](#)), similar to its counterpart in the atmosphere. [Rossby and Montgomery \(1935\)](#) were the first to employ a similarity scaling of the atmosphere in this two-layer model, dubbed Rossby similarity theory ([Du Vachat and Musson-Genon 1982](#); [McPhee 1981](#)). This theory predicts a universal scaling of the quadratic drag coefficient with the friction Rossby number $Ro = u_* / f z_0$ ([McPhee 1981](#)), where z_0 is the underice roughness length and u_* is the square root of the kinematic turbulent shear stress (friction velocity).

Vertical mixing of ocean heat toward the ice contributes to melting. Because the salinity of sea ice is usually far less than that of seawater ([Untersteiner 1968](#)) and the density of cold seawater is dominated by saline contraction ([Fofonoff and Millard 1983](#)), the downward mixing of meltwater implies upward buoyancy fluxes. Thus, ice melt leads to strong surface stratification, and intermediary pycnoclines can form at the bottoms of mixing layers. Turbulence is dampened in stable stratification because it has to work against gravity (e.g., [McPhee 2008](#)).

The vertically integrated solution to the Ekman equation, that is, the Ekman transport, does not depend on the eddy viscosity profile. Therefore one can reason that very stable stratification, specifically when the Ekman spiral interacts with a shallow pycnocline and eddy viscosity is reduced, will lead to large deviations from Rossby similarity scaling. Using an empirical model, [McPhee \(2012\)](#) predicts increased turning angles for shallow pycnoclines. However, this has neither been investigated for cases of surface meltwater accumulation during summer nor been quantified experimentally, as far as the authors know.

Furthermore, when the upper ocean is strongly stratified, the motion of ridged ice can lead to the generation of internal waves ([Morison et al. 1987](#); [McPhee and Kantha 1989](#)). Thus, energy is partitioned between the turbulent and internal wave spectra, and turbulent mixing of scalars is inhibited since internal waves do not transport mass (e.g., [Olbers et al. 2012](#)). However, ridged ice will also enhance turbulent mixing by increased stirring (e.g., [Skylingstad et al. 2003](#)).

In an inhomogeneous ice cover characterized by expanses of open water and thin, ponded ice, other freshwater sources may become important. This may, for example, be additional lateral melt of ice floes,

collection of meltwater in leads and underice ponds ([Holland 2003](#)), or percolation of freshwater through the ice matrix (e.g., [McPhee 2008](#)). Thus, the heat and salt balance at the ice–ocean interface is altered, modifying vertical fluxes of heat and salt as well. In the late melt season, vertical fluxes of scalars are therefore determined by a complicated interplay between turbulence, internal waves, and the modification of vertical gradients by horizontal inhomogeneities.

In recent decades, there have been drastic changes in the constitution of Arctic sea ice, which has gone from large portions of multiyear ice (ice that has survived at least one melting season) to a predominantly first-year ice cover (e.g., [Comiso 2012](#); [Maslanik et al. 2007](#)) dominated by a more pronounced seasonal melt/freeze cycle. The ice drift has sped up (e.g., [Hakkinen et al. 2008](#)), and the overall pressure ridge characteristics are likely to change since first-year and multiyear sea ice exhibit different ridge properties ([Wadhams and Toberg 2012](#)). Ridges, in turn, are important for the ice–ocean drag ([Lu et al. 2011](#)), and changes in their overall characteristics might change the ice–ocean interaction. The area north of Svalbard is predominantly covered by young ice and therefore an ideal test bed for what is likely to become the prevalent ice type in the Arctic ([Renner et al. 2013](#)). At the same time, we set out to investigate the validity of IOBL concepts in a regime of surface meltwater accumulation and to quantify its effects on turbulent ice–ocean fluxes of heat and momentum.

Instruments and data processing are described in [section 2](#). In [section 3](#), we describe the environmental conditions and present basic results. We derive a suitable parameterization of ocean–ice fluxes of heat and salt and use it to discuss the measured heat fluxes in [section 4](#), followed by a discussion of ice–ocean drag in [section 5](#). The main findings are summarized in [section 6](#).

2. Methods

a. The 2012 ICE cruise

The presented dataset was collected during an interdisciplinary cruise of the Centre for Ice, Climate and Ecosystems (ICE) at the Norwegian Polar Institute in July and August 2012 aboard the Research Vessel (R/V) *Lance*. The cruise included a 1-week ice drift station in the Nansen basin north of Svalbard with a comprehensive measurement program in the ice–ocean–atmosphere boundary layer. From 26 July to 3 August, the surveyed ice floe drifted south from 82.5° to 82°N between 20° and 22°E [see the drift map in [Hudson et al. \(2013, supplemental material\)](#)].

Hydrographic profiles of the upper 100 m were recorded with an Idronaut Ocean Seven 316 Plus CTD probe, set to sample at 3 Hz. Profiles were made from the ice two to three times a day. To measure microscale shear, temperature, and salinity in the water column, a loosely tethered, free-falling Sea & Sun Technology Microstructure Profiler MSS90L dropsonde was used (Prandke and Stips 1998). Microstructure data were collected in sets of three consecutive profiles, typically twice per day, amounting to 16 sets in total over the whole drift.

Turbulence in the IOBL was measured using a turbulence instrument cluster (TIC; see, e.g., McPhee et al. 1987) mounted on a mast and deployed at a nominal depth of 1 m under the ice–ocean interface, roughly 300 m away from the *Lance*. The cluster consisted of a Sontek 5-MHz acoustic Doppler velocimeter (ADV) and standard Sea-Bird sensors for temperature (SBE3) and conductivity (SBE4), measuring in approximately the same water volume. While the SBE3 has a response time fast enough to resolve turbulence, the SBE4 relies on its conductivity cell being flushed by the ocean current, which introduces a severe low-pass filtering effect (Sirevaag 2009). The mast is rotated a few times per day such that the sampling volume faces the incident ice-relative current to avoid distortion of the current by the mast and to optimize flushing of the SBE4. The Sea-Bird sensors were controlled through an SBE9 processing unit and an SBE11 deck unit connected to a laptop. The ADV was connected to the laptop via a Sontek Hydra processing unit. All instruments were set to a sampling frequency of 2 Hz, and the data were logged on one laptop using custom scripts following Sirevaag et al. (2010). This ensures synchronous time stamps for all instrument records.

In addition, 14 m from the TIC site, a Nortek Aquadopp 600-kHz acoustic Doppler current profiler (ADCP) was continuously measuring throughout the drift. The GPS data used for the present analysis are taken from *Lance*'s navigational system. Wind velocity and stress were logged by an eddy covariance system deployed on the ice at a height of 2.35 m above the ice surface (Hudson et al. 2013, supplemental material), roughly 30 m from the TIC site.

b. Data processing

1) GPS

Lance GPS positions were subsampled every 60 s during the times the *Lance* was moored to the floe, which it was throughout the drift except for one 4-h period. Latitude and longitude were mapped to polar stereographic coordinates to calculate the velocities as

first-order finite differences. These were smoothed by averaging in 5-min bins.

2) VERTICAL TURBULENT FLUXES

Records from the TIC were divided into 15-min intervals. For each interval, velocity data were rotated into a streamline coordinate system (u, v, w) with $\langle u \rangle$ equal to the mean speed and $\langle v \rangle = \langle w \rangle = 0$, with v remaining horizontal. Reynolds decomposition splits velocity and temperature into a mean $\langle \cdot \rangle$ and a turbulent part, where the turbulent part, denoted by a prime, is calculated by linearly detrending the data and has zero mean. The correlation of the turbulent fluctuations of temperature and horizontal velocity with the turbulent vertical velocity then yields the vertical transports of heat and horizontal momentum:

$$F_H = \rho_w c_w \langle w' T' \rangle, \quad \text{and} \quad (3)$$

$$\hat{\tau} \equiv u_*^2 = \sqrt{\langle u' w' \rangle^2 + \langle v' w' \rangle^2}, \quad (4)$$

where ρ_w and c_w are density and heat capacity of seawater, respectively, and u_* is the turbulent friction velocity, a velocity scale of the turbulent eddies. Since 1 m below the ice–ocean interface is usually in the constant stress (surface) layer (e.g., McPhee 1981), we can assume $\hat{\tau}$ to be the turbulent ice–ocean stress. In the higher-frequency ranges > 0.03 Hz during the first half of the drift, low signal amplitudes in the ADV data indicate a low signal-to-noise ratio, most likely due to low levels of backscatterers in the water as evidenced by concurrently low levels of biological productivity (P. Assmy 2013, personal communication). This necessitates filtering the ADV data prior to calculating the covariances. Using a digital first-order Butterworth low-pass filter, a cutoff frequency of 0.0316 Hz was found to be the best trade-off between losing higher-frequency data and reducing noise. This is evidenced by the minimal effect it has on $\langle w' T' \rangle$ values, while it significantly lowers the u_* estimates during times of low data quality (not shown), strongly suggesting that it is indeed noise that is uncorrelated with temperature measurements.

3) THE TOTAL ICE–OCEAN STRESS

Ice–ocean stress can also be estimated from the momentum balance of sea ice. In free drift (i.e., neglecting internal ice stresses) and neglecting the small terms related to atmospheric pressure gradient and sea surface slope, one has the momentum budget (e.g., Leppäranta 2011, chapter 6):

$$\tau_a + \tau_w + \tau_{\text{cor}} = h \rho_i \mathbf{U}_{\text{ice}}. \quad (5)$$

The term τ_a is the wind stress, h is the ice thickness, ρ_i is the ice density, \mathbf{U}_{ice} is the ice velocity, $\tau_{\text{cor}} = -ifh\rho_i\mathbf{U}_{\text{ice}}$ is the Coriolis force, and $\dot{\mathbf{U}}_{\text{ice}}$ is the ice acceleration. The equation $\tau_w = \rho_w u_{*w} \mathbf{u}_{*w}$ is the (total) ice–ocean interface stress, composed of turbulent shear stress, form drag, and internal wave drag. The friction velocity \mathbf{u}_{*w} points in the same direction as τ_w . Based on GPS and wind stress data, it is thus possible to estimate the ocean stress from Eq. (5). In the following, boldface \mathbf{U} , $\boldsymbol{\tau}$, and \mathbf{u}_{*} denote vector quantities, given by complex numbers as before, whereas U , τ , and u_{*} denote their magnitudes.

4) MICROSTRUCTURE DROPSONDE

Data were processed following Fer (2006). A noise level similar to the one found there is expected also for the present dataset ($\sim 10^{-9} \text{ W kg}^{-1}$), as we now used the somewhat longer and heavier MSS90L model with a descent rate of $0.5\text{--}0.6 \text{ m s}^{-1}$. Following Yamazaki and Osborn (1990), dissipation of turbulent kinetic energy was estimated from the measured microscale shear as

$$\epsilon = 7.5\nu\langle(\partial_z u')^2\rangle, \quad (6)$$

where ν is the molecular viscosity of seawater and $\partial_z u'$ is the turbulent shear. The buoyancy frequency is calculated as $N = \sqrt{-g\partial_z \rho/\rho}$, where g is the gravitational acceleration. Results were averaged in vertical bins of 0.5 m. Because there was one set that contained only two casts, in one of which the dissipation was entirely below the noise level, we have 15 sets with three casts each, and one set containing one cast.

5) WIND

Wind, air temperature, and wind stress data were provided by S. Hudson, computed from the eddy covariance measurements with EddyPro (version 4.1.0, LI-COR Biosciences) for 30-min averaging intervals using the standard settings (Hudson et al. 2013, supplemental material). Wind stress is calculated in a streamline coordinate system according to $\tau_a = \rho_a \langle u' w' \rangle$, where ρ_a is the density of air, and τ_a is parallel to wind direction (S. Hudson 2013, personal communication). Wind stress data points with wind approaching from the instrument mast or the ship were discarded. Since the weather mast deployed on the ice was not equipped with a compass, determination of its heading is subject to considerable uncertainties. This was accounted for by using wind speed and wind stress from the sensors on the ice and adjusting the heading to match the mean value of the wind measured by *Lance*'s onboard system, located at roughly 25 m above water (T. I. Karlsen 2013, personal communication), and adding the floe rotation. The amount of Ekman turning between the two heights was

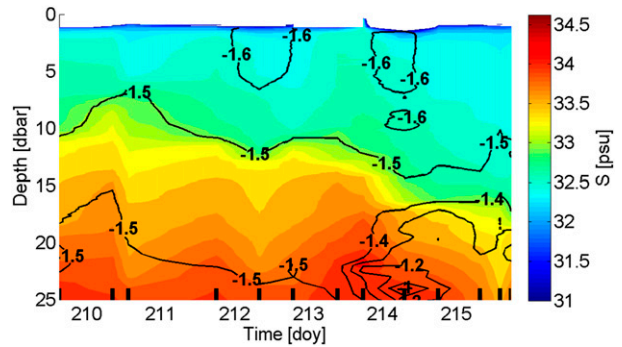


FIG. 1. Underice hydrography sampled with the Idronaut. Shading is salinity S ; the contours are temperature T ($^{\circ}\text{C}$). The black marks at the bottom indicate casts. Note that there are strong gradients in the uppermost meter under the ice–ocean interface that are not displayed here.

deemed negligible for our purpose, reasoning that typical Arctic summer conditions indicate only weakly stable stratification in the first tens of meters (Grachev et al. 2005).

3. Results

The experiment site was established on an ice floe with an average thickness of 0.8 m and a diameter on the order of 500 m (Hudson et al. 2013). Air temperatures ranged between -2° and 2°C during the whole drift (not shown). Consistent with late summer conditions, the ice cover was in an advanced stage of melt, with large expanses of ponded ice and open water. Melt progressed noticeably during the course of the drift. Judging from helicopter surveys of the area, the ice floe was representative for the region (Hudson et al. 2013). The TIC was deliberately deployed within 20 m of a pressure ridge to study its effects on the locally measured turbulent fluxes. According to a diver survey, the ridge keel reached roughly 2 m under sea level at its end points and down to 3.5–4 m in the center (H. Hop 2012, personal communication). Headings are given turning clockwise from 0° in the north and denote the direction of motion. Time is given in decimal day of the year (doy), where, for example, doy 208.5 in 2012 would be 1200 UTC 26 July.

a. Hydrography in the IOBL and close to the ice–ocean interface

Stratification was stable even in the uppermost 10 m, with salinities of 32 psu in the upper meters, reaching around 33 psu before the pycnocline starts (Fig. 1). The pycnocline is at times rather vague and not a distinct feature in the water column, but it is located between 10–15 m in the first and around 15–20 m in the second half of the drift. Temperatures measured at the TIC

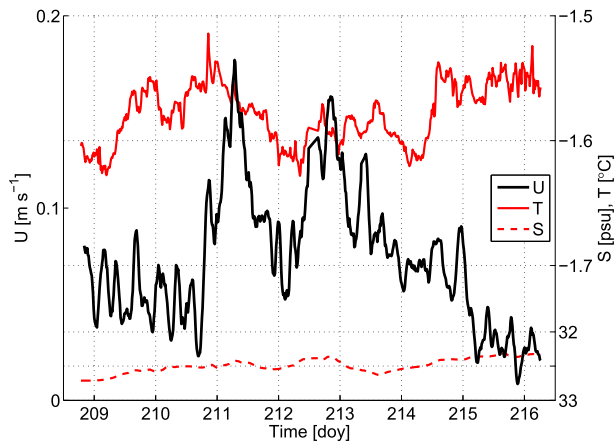


FIG. 2. Bulk variables from the TIC: ice-relative current speed U , temperature T , and salinity S . Note that S is also plotted in the temperature scale in terms of the freezing temperature $T_f = -0.0548^\circ\text{C}\text{psu}^{-1} \cdot S$, so that the distance $T - S$ between the red lines is the elevation over local freezing.

were in the range from -1.65° to -1.5°C , well above but within 0.3 K of freezing. The salinity measured at the TIC and thus the local freezing point varied only little; the latter was on average -1.78°C (Fig. 2).

b. Ice drift and water velocity

Wind speeds were moderate with a range of $2\text{--}8\text{ m s}^{-1}$ (Fig. 3). The wind heading was initially toward the south, making one full counterclockwise turn during the first 6 days and ending toward the south again, while the last third of the drift saw very low wind speeds in the range of $1\text{--}3\text{ m s}^{-1}$ and no clear direction. There were two periods of elevated (7 m s^{-1}) winds with steady heading during day 211 and 212–213, respectively. The 12-h running average ice drift velocity was in the range $0.1\text{--}0.2\text{ m s}^{-1}$, climbing to up to 0.4 m s^{-1} at one point with semidiurnal oscillations prevailing during the second half of the drift (Fig. 3). Averaging individual estimates of speed ratio and direction difference over the whole drift period, the ice drifted at $3.3\% \pm 0.8\%$ of the wind speed and $45^\circ \pm 20^\circ$ to the right of the wind heading. The uncertainties are given as one standard deviation.

Figure 4 shows ice-relative current speed and direction during the drift station, measured by the ADCP. Inertial oscillations have a period of roughly 12 h close to the poles and are therefore indistinguishable from semidiurnal tidal motion in short datasets, but away from the shelves in the deep basins of the Arctic, tides are generally weak with amplitudes of only a few cm s^{-1} (Padman and Erofeeva 2004). This means that the observed semidiurnal oscillations indicate inertial motion. Peak ice-relative velocities averaged over 17–22 m depth during days 211 and 213 reached $0.35\text{--}0.4\text{ m s}^{-1}$.

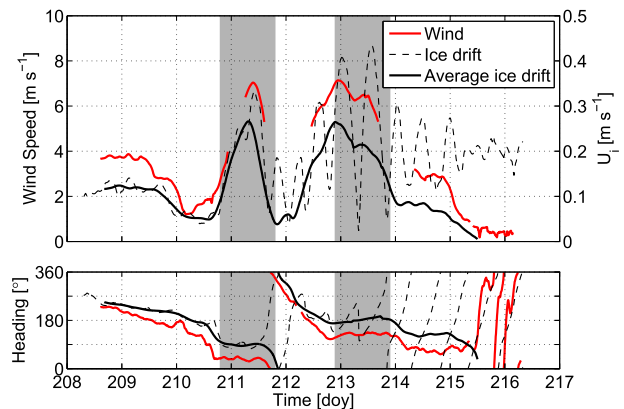


FIG. 3. Velocity of wind and ice drift U_i . (top) Speed and (bottom) direction. Black solid line is the ice drift with a 12-h running mean. The gray shading represents the time periods of the two wind events, day 210.8–211.8, and day 212.9–213.9.

At 4-m depth, the ice-relative velocity reached 0.2 m s^{-1} during day 211 and 212–213, but stayed below 0.1 m s^{-1} most of the remaining time. The absolute velocity (ice-relative current plus GPS-based ice drift) below about 15 m exhibits no inertial component throughout the drift, and averaging over the interval 17–22 m gives a good indication of the ice drift relative to the undisturbed ocean. The results do not depend on the precise choice of this averaging interval. The ice-relative current measured at the TIC briefly climbs over 0.15 m s^{-1} during day 211 and 212–213 and exhibits a pattern similar to the ADCP measurements at 4-m depth (Fig. 2).

We focus on two periods of elevated wind velocities with steady heading, that is, day 210.8–211.8 and 212.9–213.9,

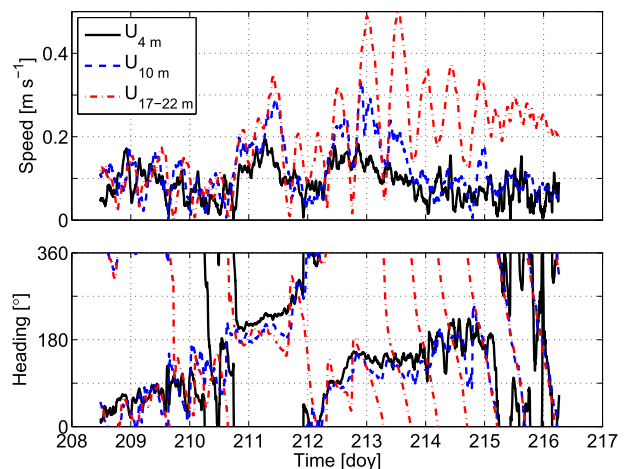


FIG. 4. Relative currents as (top) speed and (bottom) magnetic heading. The terms $U_{4\text{m}}$, $U_{10\text{m}}$ and $U_{17\text{--}22\text{m}}$ are currents at 4 m, 10 m, and averaged over 17–22 m, respectively.

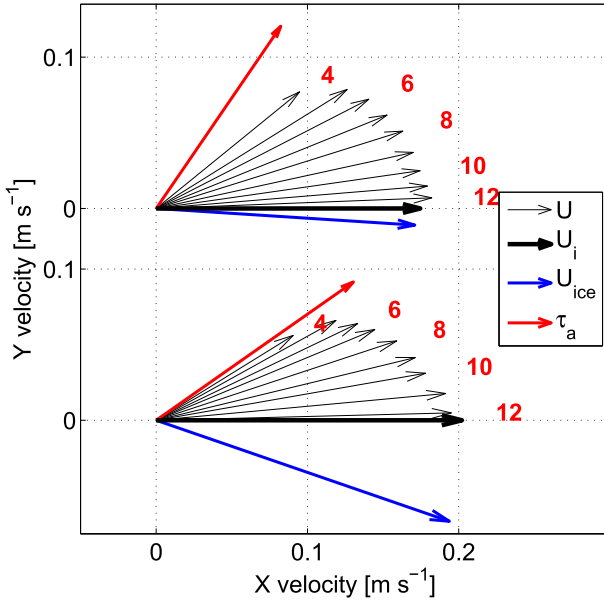


FIG. 5. Mean hodographs of the two analyzed periods, rotated such that U_i (the ice drift relative to the ocean calculated as the average over 17–22 m) points in the x direction. The upper hodograph represents the first wind event, doy 210.8–211.8, and the lower hodograph represents the second wind event, doy 212.9–213.9. Black, thin arrows signify ice-relative velocities with approximate depths in meters. The blue arrows are the actual ice drift U_{ice} . Wind stress τ_a (solid red arrow) is displayed in $\text{kg m}^{-1} \text{s}^{-2}$.

dubbed the first and second wind event, respectively. Each duration was chosen to be 24 h to minimize the effect of diurnal, semidiurnal, and inertial oscillations. Figure 5 shows period-mean hodographs for the two wind events. Assuming no additional turning above the uppermost measurement level of roughly 4 m, that is, around 3 m below the ice, they indicate turning angles of $\phi = 39^\circ$ and 32° , respectively.

c. Ice–ocean stress and heat flux

Using representative values of $\rho_i = 900 \text{ kg m}^{-3}$ (Timco and Frederking 1996) for ice density, $f = 1.44 \times 10^{-4} \text{ s}^{-1}$ at 82°N and an ice thickness of $h = 0.8 \text{ m}$, the ice–ocean stress τ_w can be calculated from Eq. (5) assuming free drift. Kwok et al. (2013) show that our study area is generally very close to free drift in the summer. Furthermore, in the present study, the correlation coefficient between wind speed and 12-h average ice drift speed is 0.98 for the whole drift period including a variety of wind directions, indicating that drift was indeed close to free. Seeing that the Coriolis and the acceleration terms turn out to play minor roles compared to the wind stress through most of the drift, the result is stable even against large deviations from the chosen density value. Figure 6 shows different terms of the momentum

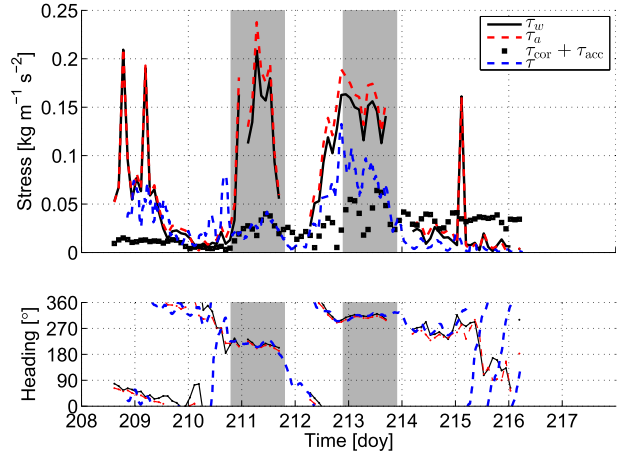


FIG. 6. Terms of the momentum budget. (top) Stress magnitudes. The thick black and red lines are ocean (τ_w) and wind (τ_a) stresses. Note that $\tau_{cor} + \tau_{acc}$ denotes the vector sum; the individual terms τ_{cor} and τ_{acc} terms have a similar magnitude (not shown). (bottom) Headings for τ_w , τ_a , and τ . The gray shading is the same as in Fig. 3.

budget and the turbulent stress estimate from the TIC. Air–ice and ice–ocean stresses are almost in balance, with only minor contributions from the acceleration and Coriolis terms until doy 214, after which they dominate the momentum budget due to strong inertial oscillation during the last 2 days (Fig. 3). The ice–ocean stress directly measured at the TIC is, on average, around 3 times smaller than the one inferred from the wind stress.

The nondimensional surface velocity $\mathbf{U}/\mathbf{u}_{*w}$ is calculated from the 24-h-averaged ice-relative velocity at 17–22 m. The ice–ocean stress is oriented along the 4-m ADCP velocity. Drag coefficient magnitude $C_D = \hat{\tau}_w/U_i$ and turning angle ϕ are steadiest during the second wind event with mean values around $C_D = 3.4 \times 10^{-3}$ and $\phi = 32^\circ$ (Fig. 7), but have large variations otherwise. Heat fluxes at the upper TIC are generally positive with a mean value of roughly 10 W m^{-2} , peaking at 50 W m^{-1} during a 1-day period of elevated heat fluxes on doy 212 and 213 (Fig. 8). The friction velocity follows a similar

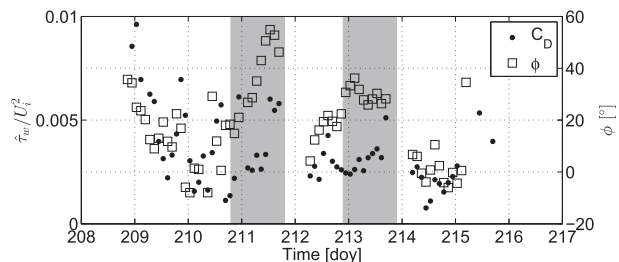


FIG. 7. Drag coefficient magnitude $C_D = \hat{\tau}_w/U_i^2$ (dots) and turning angle ϕ (squares). The gray shading marks the periods used in Fig. 5.

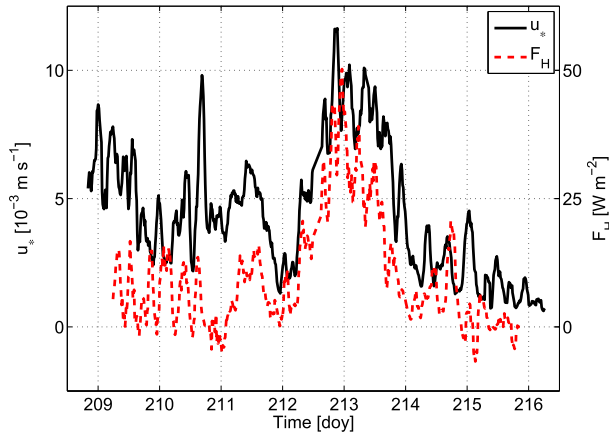


FIG. 8. Friction velocity u_* (solid black line) and heat flux F_H (dashed red line) estimated from the TIC.

pattern, climbing to 1 cm s^{-1} on day 213 (in the same place).

4. Ice–ocean heat flux

a. Modeling interface heat and salt fluxes

The ice–ocean fluxes across the thin molecular sub-layer right beneath the ice–ocean interface are set by the turbulent boundary layer underneath (McPhee et al. 1987). Since we lack measurements of turbulent salt flux (a simultaneously deployed SBE7 conductivity micro-structure sensor malfunctioned), we can only use heat flux observations to constrain underice melt. By heat and salt conservation at the interface, however, the vertical fluxes of heat and salt are experimentally constrained. The goal of this section is to assess how the oceanic heat flux is affected by the salt balance at the interface. Thus, we will be able to interpret heat flux measurements without direct measurements of salt flux. Following Schmidt et al. (2004) and with $\delta T = T_m - T_0$ and $\delta S = S_m - S_0$, the temperature and salinity difference between the ocean side of the interface (T_0, S_0) and the far-field mixed layer (T_m, S_m), we can parameterize the kinematic heat and salt fluxes as

$$\langle w'T' \rangle = \alpha_T u_* \delta T, \quad \text{and} \quad (7)$$

$$\langle w'S' \rangle = \alpha_S u_* \delta S, \quad (8)$$

with constant transfer coefficients $\alpha_{T,S}$. Positive heat and salt fluxes are upward (into the ice). At the interface, we close the system of equations with a linear freezing point relation

$$T_0 = T_f(S_0) = -mS_0, \quad (9)$$

where $m = 0.055^\circ\text{C psu}^{-1}$. If we assume that the difference between the specific energies of ice and meltwater is the latent heat, which means an error of at most a few percent (Schmidt et al. 2004), heat and salt conservation at the interface can be approximated as

$$\langle w'T' \rangle = Q_L w_0 + q_c, \quad \text{and} \quad (10)$$

$$\langle w'S' \rangle = w_0(S_0 - S_i) + \Sigma. \quad (11)$$

The value $Q_L = L/c_w$ is the ratio of latent heat to heat capacity of seawater and q_c the (upward) conductive heat flux through the ice divided by $\rho_w c_w$. The term S_i is the ice salinity close to the interface, and the melt rate w_0 is related to the interface velocity \dot{h} , that is, the underice change in ice thickness, by $w_0 = \dot{h}\rho_i/\rho_w$. The Σ term was added as an ad hoc means to incorporate additional salt fluxes such as percolation or salt flux due to leads, underice melt ponds, and so on and is thus more general than only using the percolation velocity as is done by, for example, McPhee (1992). Equations (7) to (11) fully describe the ice–ocean heat and salt exchange. Apart from the Σ term, this exposition followed Schmidt et al. (2004).

Using Eq. (9) and $\delta T = \Delta T + T_f(S_m) - T_0$, $\Delta T \equiv T_m - T_f(S_m)$,

$$\langle w'T' \rangle = \alpha_T u_* (\Delta T + m\delta S). \quad (12)$$

Combining Eqs. (7) and (8), the salt budget becomes

$$\langle w'S' \rangle = \frac{\langle w'T' \rangle - q_c}{Q_L} (S_0 - S_i) + \Sigma, \quad (13)$$

and with Eq. (12) and $\langle w'S' \rangle = \alpha_T u_* \delta S/R$,

$$\begin{aligned} \langle w'T' \rangle &= \frac{\alpha_T u_* \Delta T + \frac{mR}{Q_L} q_c (S_0 - S_i) - mR\Sigma}{1 + \frac{mR}{Q_L} (S_0 - S_i)}, \\ &\equiv C_H u_* \Delta T + \delta q \end{aligned} \quad (14)$$

with a bulk heat transfer coefficient C_H and some heat flux offset δq caused by the conductive heat flux and Σ . Here, the ratio $R = \alpha_T/\alpha_S$ determines the strength of double-diffusive effects (e.g., Sirevaag 2009). Note that for common IOBL conditions, $S_0 - S_i \approx S_m - S_i$, such that α_T/C_H only depends on mixed layer quantities and R . For the case of a small offset δq (small q_c and Σ , that is, thick ice with snow on top or a surface temperature not too far below freezing and no salt sinks other than ice melt), this is a theoretical derivation of the empirical relation $\langle w'T' \rangle = \text{St} u_* \Delta T$, where St is the bulk Stanton

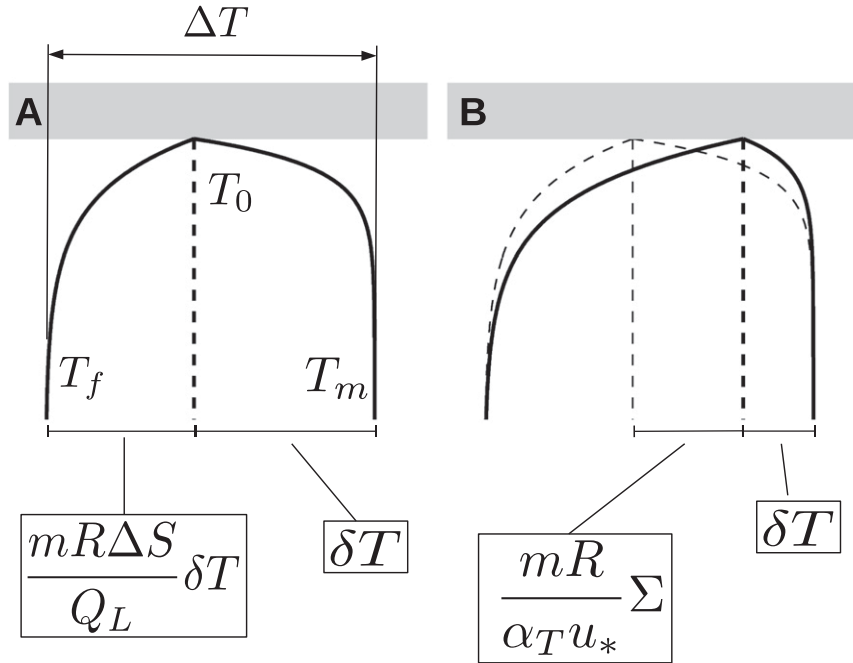


FIG. 9. Sketch explaining Eq. (14). (left) $\delta q = 0$, so $\Delta T = (1 + mR\Delta S/Q_L)\delta T$. (right) An additional salt flux Σ increases the interface temperature. While T_f and T_m are held constant, δT decreases, thus lowering the ice–ocean heat flux.

number (McPhee 1992). This is in line with Notz et al. (2003), who have found that the bulk Stanton number parameterization is quite accurate for thick ice when considering a one-dimensional model not using a Σ term. Equation (14) is illustrated in Fig. 9 using two scenarios, one where $\delta q = 0$ and the other one with a Σ term.

b. Bulk heat transfer coefficient

Equation (14) is fitted to the data for day 212.4–214.7, dominated by elevated wind speeds with a steady direction and a wide range of friction velocities. The reasoning here is that the constant wind direction and initially strong winds facilitate adjustment to a steady local forcing rather than domination by the variation of other parameters. While the regression describes the data very well during the second wind event, heat fluxes are reduced during the other times and do not follow a similar easily visible trend (Fig. 10). Fixing the slope C_H , this would mean that δq varies considerably.

We infer a slope of $C_H = 0.0055$ from the second wind event and an average heat flux reduction of $\rho_w c_w \delta q = -10 \text{ W m}^{-2}$ for the whole drift. From ice cores, we infer a conductive heat flux of $q_c = -8 \times 10^{-7} \text{ K m s}^{-1}$. Its contribution to the δq term is one order of magnitude smaller than the δq term and therefore negligible. The additional salt flux in the interface budget is $\Sigma = 1.3 \times 10^{-6} \text{ psu m s}^{-1}$ for the period we used for the regression. Having fixed the slope $C_H = 0.0055$, we can calculate Σ

for every data point and calculate the corresponding salt flux using Eq. (13). The inferred average buoyancy flux becomes $\langle w'b' \rangle = g(a_S \langle w'S' \rangle - a_T \langle w'T' \rangle) = 2.6 \times 10^{-8} \text{ m}^2 \text{ s}^{-3}$ instead of $9 \times 10^{-9} \text{ m}^2 \text{ s}^{-3}$ if the Σ term had been excluded. Here, a_S and a_T are the saline contraction and thermal expansion coefficients. Note that the total ice energy budget, which was measured by Hudson

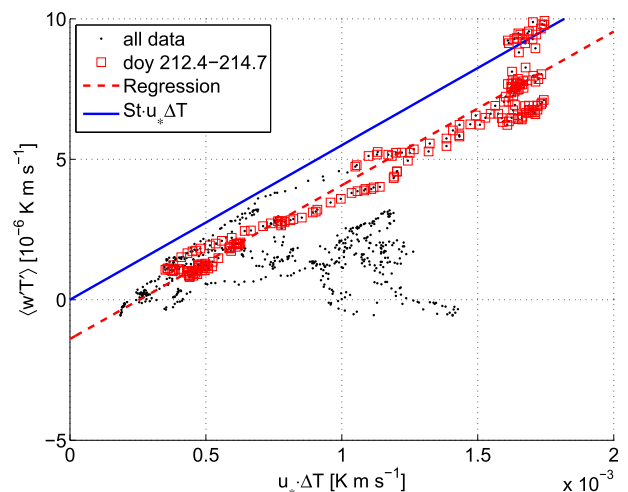


FIG. 10. Vertical turbulent heat flux $\langle w'T' \rangle$ plotted against $u_* \Delta T$. Red dashed line signifies linear regression to the red squares. Blue solid line signifies the Stanton number prediction $\langle w'T' \rangle = 0.0055 u_* \Delta T$.

et al. (2013), presents an upper boundary for the buoyancy flux and yields $\langle w'b' \rangle_{\max} \approx 5 \times 10^{-8} \text{ m}^2 \text{ s}^{-3}$.

McPhee (1992) finds a bulk Stanton number $St = \langle w'T' \rangle / u_* \Delta T \approx 0.0056$ over a large range of ice types and friction velocities (McPhee 2008). This especially means that there is no dependence on the underice roughness z_0 . Our value for $C_H = 0.0055$ does indeed compare favorably with $St = 0.0056$. From seven ice cores, we infer $S_i = 4$ psu, which is plausible even for first-year ice when considering that it was late in the melting season. With $R = 35$ (Notz et al. 2003), $S_m = 32.5$ psu and $Q_L = 68$ K [following the formulas by Fofonoff and Millard (1983)]:

$$1 + \frac{mR}{Q_L}(S_0 - S_i) \approx 1 + \frac{mR}{Q_L}(S_m - S_i) = 1.75, \quad (15)$$

so $\alpha_T \approx 0.0095$ and $\alpha_S \approx 0.00027$. If instead a double-diffusive ratio of $R = 70$ [the other end of the theoretical range according to Notz et al. (2003)] is used, $\alpha_T = 0.014$ and $\alpha_S = 0.00019$.

Sirevaag (2009) found $\alpha_T = 0.013$, $\alpha_S = 0.0004$, and $R = 33$ from directly solving the three-equation system with heat and salt flux estimates from a similar TIC setup during a period of rapid melting, but not considering a Σ term.

It should be noted that instead of introducing a salt flux offset Σ , the same effect [offset of the heat flux from its Eq. (14) prediction] can be achieved by introducing an additional (downward) heat flux Θ , which is related to Σ by the scaling $mR/[1 + (mR/Q_L)(S_m - S_i)]$ or any linear combination thereof. This could, for example, represent solar heat stored in leads, which, just like freshwater, accumulates during periods of low wind stress. While the physics behind the Σ term is not clear, the average heat flux reduction by 50% relative to the bulk Stanton number estimate of 20 W m^{-2} is evident. Another mechanism to reduce the heat fluxes measured at the TIC level could be a vertical structure in the insolation, which warms shallower waters more than deeper, thus counteracting the heat flux. To find an absolute upper bound for this effect, we assume a steady-state temperature and an exponential decay of the insolation: $F = F^0 \exp(-\gamma z)$, where $F^0 = 20 \text{ W m}^{-2}$ is the drift average insolation reaching the underice ocean (Hudson et al. 2013) and $\gamma = 0.07$ is a representative extinction coefficient for clear water in the Nordic Seas (Sakshaug 2004). The maximum reduction in heat flux measured at 1 m below the ice–ocean interface is then $\Delta \langle w'T' \rangle = F^0 [1 - \exp(-\gamma z)] / c_w \rho_w \approx -1.5 \text{ W m}^{-2}$, which is relatively small even during the second wind event, when the offset was comparably small (Fig. 10). Note that a realistic value for the heat flux reduction by insolation is probably even smaller, both since the water is

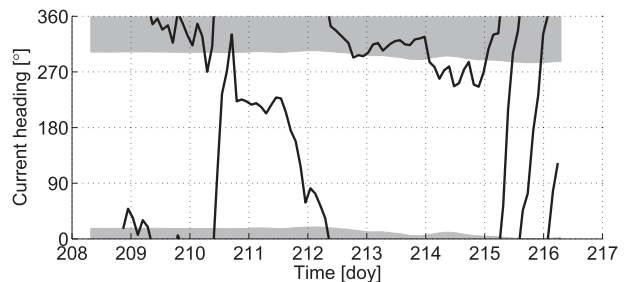


FIG. 11. Current direction 1 m under the ice from the upper TIC. Shaded region shows the estimated range of headings directly affected by the ridge.

heated and since the ice–ocean interface provides an ice bath condition, thus preventing a steady state.

Note that for $R = 1$, Eq. (14) predicts $\alpha_T = C_H$, since then $(mR/Q_L)(S_0 - S_i) \ll 1$. This is also consistent with the findings of Cole et al. (2014), who find $C_H = 0.0124$ for winter measurements in a regime with no double-diffusive effects (i.e., $R = 1$). Furthermore, they find that their data are best described by a heat flux parameterization $\langle w'T' \rangle = C_H u_* \Delta T - m \langle w'S' \rangle$. For a scenario with δq and $\delta S \approx 0$ (as is appropriate for thick, freezing ice; see, e.g., MCPhee 2008), their parameterization is exactly the same as Eq. (14), since then $\Sigma = \langle w'S' \rangle$. In such a scenario, Σ quantifies the brine rejection from freezing sea ice. This short example demonstrates that even though Eq. (14) was tested with respect to sea ice melt in which double diffusion probably plays a role, it might be applicable to a wider range of conditions.

5. Ice–ocean stress

a. Ridge keel effect on local turbulence measurements

Figure 11 shows the mean ice-relative current heading, measured at the TIC, together with the range of the current headings possibly affected by the wake behind the ridge. The small variation in that range stems from the rotation of the floe, estimated from the heading of the bow of the R/V *Lance* when it was moored to the floe. Note that the gray envelope is based purely on aerial photography to estimate the heading of the end points of the ridge as seen from the TIC, and no physical evaluation of wake effects or similar has been made. While the momentum budget estimate in Fig. 6 suggests the same amount of ice–ocean stress for both wind events ($\approx 0.14 \text{ kg m}^{-1} \text{ s}^{-2}$), the TIC-based stress is 2–4 times higher during the second period (day 212.7–213.5) than during the first, meaning roughly a 40% to 100% increase in friction velocity and thus vertical fluxes of heat and salt.

This increase in turbulent friction velocity during the second wind period might in part be due to longer and

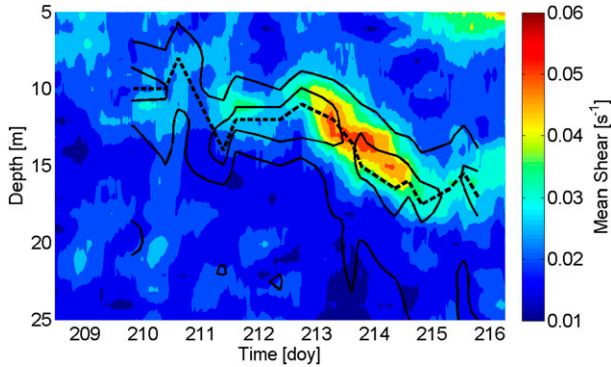


FIG. 12. The 12-h running average of shear magnitude, calculated from ADCP data. Dashed line shows the location of maximum N^2 , inferred from MSS dropsonde data. Contour lines at $N^2 = 5$ and $10 \times 10^{-4} \text{ s}^{-2}$.

sustained mixing. However, it seems to be mostly due to the current coming from the pressure ridge during that period, which enhances “stirring” (Fig. 11). This observation is not unexpected and in line with what has been observed in numerical simulations by Skyllingstad et al. (2003). Shaw et al. (2008) report a roughly 20% decrease in U/u_* when the current was approaching from a pressure ridge roughly 25 m away, which translates to a relative increase in turbulent stress by roughly 60% and is thus consistent with our findings. Note that the presence of the ridge does not influence the conclusions of the previous section as it was the mere scaling $\langle w'T' \rangle \sim u_*$ that mattered there.

b. Do inertial oscillations contribute to mixing in the pycnocline?

The average turbulent ice–ocean stress estimated from the TIC is roughly $1/3$ of the ice–ocean stress estimated from the air–ice stress. The IOBL is strongly stratified even in the uppermost meters, and taking the ridge close to the TIC (with a keel depth of 4 m) as representative for ridges in the area during our study, we see that keel depths are about $1/3$ to $2/3$ the depth of maximum stratification, thereby possibly exciting internal waves (Figs. 1, 12). It is thus possible that the discrepancy is due to internal wave drag (e.g., McPhee and Kantha 1989), but other effects like form drag could also play a role. Increasing the length of the Reynolds averaging intervals to several hours does not drastically change the Reynolds stress estimates (not shown), which shows that any drag mediated by the internal wave field is transported at far lower frequencies or further down in the water column and thus does not contribute to mixing close to the surface.

One might hypothesize that inertial shear contributes to turbulent mixing further down, as internal wave

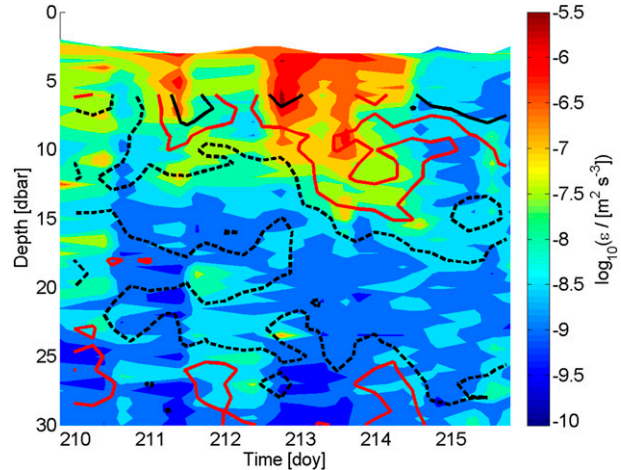


FIG. 13. Dissipation of turbulent kinetic energy from microstructure dropsonde data. Contour lines indicate Richardson number $Ri = 1$ (dashed black), 0.5 (red), 0.25 (solid black).

energy is radiated downward, where wave breaking could occur. This layer of increased shear between the upper-oscillating and the lower-nonoscillating layer is around 10–20 m, as is evidenced by Fig. 12. However, most of the dissipation is located above the region of maximum stratification (Fig. 13). Note how well the region of maximum shear magnitude corresponds to the region of maximum N^2 , and how the shear magnitude is connected to the amplitude of the inertial oscillations (Fig. 3). There is a strong correlation between total dissipation in the water column (integrated from 2.5-m depth to twice the depth of maximum N^2) and the 12-h mean ice drift (Fig. 14). No dependence on the actual ice

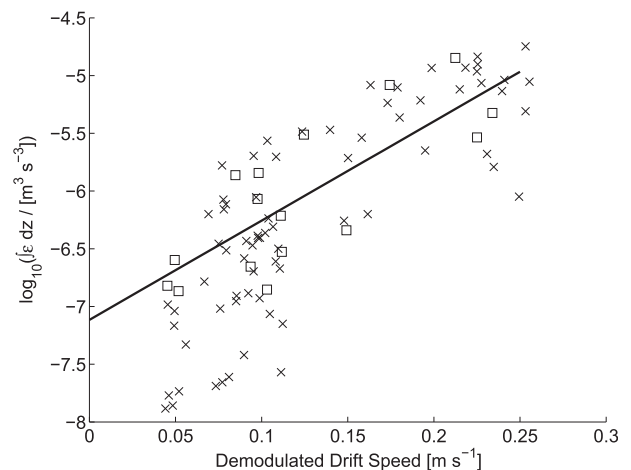


FIG. 14. Squares are the dissipation integrated from 2.5 dbar down to twice the depth of maximum N^2 , plotted against the demodulated ice drift speed (squares). Solid line is the linear regression to integrated dissipation. Crosses are the work done by demodulated ice drift on turbulent stress (see text).

drift including inertial oscillations, or the phase of the inertial oscillation, was found (not shown). In fact, for larger integrated dissipation, relatively less of it is located progressively deeper down, which is valid particularly across the 10–20-m range (not shown). This indicates strongly that wind energy input, as is represented by the noninertial ice drift, is the dominant source of turbulent small-scale mixing. The wind work of the demodulated ice drift on the turbulent stress is $\hat{\tau}U_i \cos(\phi)$, where ϕ is the turning angle between surface stress and velocity (Fig. 7). This estimate is in good agreement with the integrated dissipation, corroborating the hypothesis that the mixed layer small-scale mixing does not contain contributions from other sources than wind-driven turbulence (Fig. 14). Thus, we conclude that in this study, inertial oscillations did not significantly enhance turbulent mixing in the pycnocline.

The findings of, for example, McPhee (1978) stress that a mixed layer oscillating as a slab in phase with the ice is not an appropriate description because it would result in too high stresses at the mixed layer base. The present results indicate that even if there is such a region of enhanced shear, this contribution is small relative to the wind-driven mixing above. One may speculate that since the regions of enhanced shear coincide with the regions of strong stratification, buoyancy consumption counteracts shear production of turbulent kinetic energy just enough to make this effect very small. Indeed, profiles of Richardson number $Ri = N^2/Sh^2$, where Sh is the magnitude of vertical shear of horizontal velocity and both Sh and N^2 are estimated on a 1-m grid, reveal that the high Sh^2 is largely compensated for by high N^2 (Fig. 13), such that the Richardson number is mostly even greater than 1 throughout the pycnocline, indicating that turbulence is suppressed (see, e.g., Grachev et al. 2013).

c. Drag coefficients

Using the total ice–ocean kinematic stresses τ_w , we find $C_D = \hat{\tau}_w/U_i^2 = 3.8$ and 3.4×10^{-3} for the first and second wind events, respectively. Based on the turbulent stress τ , we find $\hat{\tau}/U_i^2 = 0.85 \times 10^{-3}$ for the first wind event (for the second, the estimate is distorted by the presence of the pressure ridge). Recall that the turning angles are around $\phi = 39^\circ$ and 32° for the first and second period, respectively (Fig. 5).

For the 1975 Arctic Ice Dynamics Joint Experiment (AIDJEX) project in the pack ice of the central Beaufort Sea, McPhee (1979) found a mean drag coefficient of 5.5×10^{-3} and a turning angle of 23° . Their ice–ocean stress estimates were based on a sea ice momentum balance similar to the one in the present article, using a quadratic wind stress parameterization. For the

Surface Heat Budget of the Arctic Ocean (SHEBA), McPhee (2008) reports a drag coefficient of 5.6×10^{-3} and a turning angle of 25.9° , based on estimates of turbulent ice–ocean shear stress. McPhee et al. (1987) find a turning angle of around 33° in the marginal ice zone in the Greenland Sea. We can conclude that the total ice–ocean drag is roughly in the range of what we would expect in the Arctic based on these earlier measurements, whereas the turbulent stress yields only a fraction of that. However, these measurements were made in different hydrographic conditions and ice types and are therefore not directly comparable to our results.

d. Rossby similarity theory

To put the results into a larger perspective and to compare measurements for different ice roughness and turbulent stresses, we can use Rossby similarity theory. This analytical theory incorporates a model of the turbulent IOBL to predict how the quadratic drag coefficient varies with the friction Rossby number Ro .

McPhee (1981) coupled this IOBL model to a buoyancy flux scaling to decrease the eddy viscosity with increasing buoyancy flux and arrives at

$$\frac{\mathbf{U}}{\mathbf{u}_*} = \frac{1}{\kappa} [\log(Ro) - A(\langle w'b' \rangle_0) \pm iB(\langle w'b' \rangle_0)], \quad (16)$$

where \mathbf{U} is the surface velocity relative to the velocity of the undisturbed ocean, and \mathbf{u}_* is the surface friction velocity (McPhee 2008, chapter 4). The term κ is the Von Kármán constant ($=0.4$), and the minus sign is for the Northern Hemisphere. The terms A and B are universal functions and depend only on other constants and the interface buoyancy flux $\langle w'b' \rangle_0$. For neutral stratification, that is, $\langle w'b' \rangle_0 = 0$, $A \approx 2.3$ and $B \approx 2.1$ (McPhee 2008). The value z_0 is the roughness length and is defined as the integration constant in the “law of the wall” $\kappa U/u_* = \log(z/z_0)$ (e.g., Morison and McPhee 2001). In laboratory experiments, it has been found to correspond to roughly $1/30$ of the height of typical roughness element of the surface bounding the flow. Neutral-stability Rossby similarity was found to describe the 1975 AIDJEX data significantly better than a quadratic drag law (McPhee 1982), with an effective exponent of $u_*^2 \sim U^{1.83}$. For the stratified case, data are even sparser, but McPhee (2008) reports Eq. (16) to be in good agreement with the atmospheric Wangara data (Clarke and Hess 1974).

For a given z_0 and $\langle w'b' \rangle$, Eq. (16) predicts the drag coefficient $(\hat{\tau}/U)^2$ and turning angle $\phi = \arg(\mathbf{U}/\mathbf{u}_*)$. Using the law of the wall, U/u_* as measured at the TIC, and a criterion $u_* > 6 \times 10^{-3} \text{ m s}^{-1}$ to get the data points with as fully developed turbulence as possible and to

minimize the influence of the stratification, we arrive at a roughness length of $z_0 = 1$ cm. Figure 15 displays the data of Fig. 7 as a function of u_{*w} . It also includes Rossby similarity predictions for $\langle w'b' \rangle = 0$ and $10^{-8} \text{ m}^2 \text{ s}^{-3}$. One has to take into account that at low friction velocities, U/u_{*w} is unreliable since some stress is required to force the water column into a steady-state situation. Using the square root of the total kinematic ice–ocean stress u_{*w} instead of the turbulent friction velocity u_* , Rossby similarity predicts the magnitude of the drag coefficient fairly well, but it should be noted that Rossby similarity was devised and tested as a model of the *turbulent* boundary layer. It is not clear whether the good numerical performance is coincidence for the observed parameter range or if it reflects a mechanism whereby a possibly increased internal wave drag compensates for the reduction of turbulent shear stress. However, Rossby similarity cannot explain the turning angles for the present dataset (Fig. 15).

e. Correcting the turning angle with the Ekman transport

Rossby similarity assumes a not too strongly varying eddy viscosity, which means that it cannot directly account for the shallow pycnoclines. Since the pycnocline, or near-surface strong stratification, limits the vertical extent of the Ekman spiral, it is “compressed” into the water column above. The depth-integrated velocity

$$\int_{-\infty}^0 \mathbf{U} dz = \frac{\hat{\boldsymbol{\tau}}_0}{if}, \quad (17)$$

where $\hat{\boldsymbol{\tau}}_0 \equiv u_{*0} \mathbf{u}_{*0}$ is the kinematic surface stress, is always at a right angle to the interface stress and proportional in magnitude and does not depend on the pycnocline depth. A higher Ekman transport distributed over the same water depth can only be accomplished by a larger turning angle or disproportionately larger velocities or a combination thereof. In fact, the turning angle in Fig. 15 even seems to increase with increasing u_* , contrary to Rossby similarity predictions and in line with the reasoning above. Indeed, we do not observe significant turning below roughly 12 m (Fig. 5).

McPhee (2012) modeled this effect by solving the steady Ekman equation using an empirical eddy viscosity profile with the so-called steady local turbulence closure model. While the drag law for a pycnocline at a depth of 40 m compares favorably to Rossby similarity estimates, a pycnocline at 20 m leads to a considerable increase in turning angle from its Rossby similarity estimate for large u_* values. The present findings support that study and even extend the validity of the statements to more extreme situations of near-surface stratification.

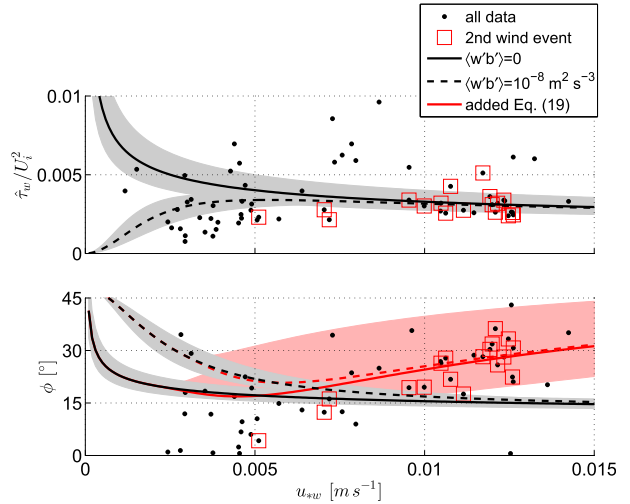


FIG. 15. Drag coefficient magnitude $C_D = \hat{\tau}_w/U_i^2$ and turning angle ϕ as a function of u_{*w} . Solid black line is the Rossby similarity estimate for $\langle w'b' \rangle = 0$, $z_0 = 1$ cm, envelope $z_0 = 0.5 - 2$ cm. Dashed black line is the estimate for $\langle w'b' \rangle = 10^{-8} \text{ m}^2 \text{ s}^{-3}$, $z_0 = 1$ cm, and envelope $\langle w'b' \rangle = 0.5 - 2 \cdot 10^{-8} \text{ m}^2 \text{ s}^{-3}$. Red lines are the correction from Eq. (19) added for $d_p = 10$ m, red envelope $d_p = 5 - 15$ cm.

To account for the increase in turning angle as an effect of the shallow pycnocline, we can consider the integrated Ekman equation [Eq. (17)]. It is solved by the ansatz

$$\mathbf{U}(z) = \mathbf{U}_0 \exp\left(\frac{if\mathbf{U}_0 z}{\boldsymbol{\tau}_0}\right), \quad (18)$$

with surface velocity \mathbf{U}_0 . Integrating only from some fixed depth $-d_p$ (the pycnocline, say) to the top of the Ekman layer, we are off by an angle

$$\arg \left[1 - \exp\left(-\frac{\sqrt{if} d_p}{u_{*0} \sqrt{C_D}}\right) \right], \quad (19)$$

where we use that $\hat{\boldsymbol{\tau}}_0/\mathbf{U}_0 = \sqrt{i} \hat{\tau}_0/U_0$ for an Ekman spiral without logarithmic surface layer. Equation (19) is therefore a first-order correction to the classical Ekman spiral solution. Figure 15 displays the Rossby similarity estimates also with this correction added. The agreement is quite good. While Eq. (19) overestimates the turning angles modeled by MCPhee (2012, his Fig. 8) by a few degrees for large velocities in his “shallow pycnocline” case, it captures the general picture (not shown). Note that a reasonable value for d_p would be the pycnocline depth minus the extent of the surface layer that is roughly $0.028 u_{*0} / \kappa f$ (in practice, this means a few meters; see, e.g., MCPhee 1981). The small negative correction to the turning angle for small u_{*w} is an artifact

of integrating far deeper than the Ekman layer extent and can be amended, for example, by setting the negative values to 0. Equation (19) can only be a first-order correction, and the complete picture requires solving the IOBL in detail. As a working assumption and a work-around for modelers, the correction Eq. (19), together with Rossby similarity, still seems to work better than constant turning angles and drag coefficients.

The fact that the drag coefficient magnitude is described quite accurately by neutral Rossby similarity even for strong near-surface stratification and a shallow pycnocline is astounding, not only because the assumption of a constant eddy viscosity profile is violated. It also highlights the fact that even for strong stratification, the actual buoyancy flux is quite moderate with only $\langle w'b' \rangle \approx 2.6 \cdot 10^{-8} \text{ m}^2 \text{ s}^{-3}$, since internal waves do not transport mass (Obers et al. 2012).

f. Applicability of the results

To put the different effects into perspective, we can calculate their respective proportions relative to the measured heat flux. If the turbulent stress alone had accounted for the total ice–ocean drag, the drift average, bulk Stanton number estimate would be $F_H = 32 \text{ W m}^{-2}$. Using the actual turbulent friction velocity u_{*s} , this figure goes down to 20 W m^{-2} . The observed heat flux, however, is 10 W m^{-2} . This means that both the reduction of the turbulent shear stress and the deviation from the bulk heat flux parameterization play a major role for the observed heat fluxes.

Given the significant heat flux reduction and especially the large turning angles, one is led to wonder how frequent the conditions observed in this study are. Toole et al. (2010) present CTD profiles sampled by ice-tethered profilers, recorded between 2004 and 2009. These show a summer mixed layer that is significantly shallower and more stably stratified relative to their AIDJEX counterparts, which is in line with the upper-ocean hydrography observed in the present dataset. The stratification we encountered during our experiment is comparable to the last 2 days in the Greenland Sea marginal ice zone described by McPhee et al. (1987) and Morison et al. (1987). There, the mixed layer depth was between 5 and 20 m and the pycnocline was as vague as in the present study and had a comparable overall stratification, which exemplifies the importance of the present scenario for melting conditions in summer. McPhee (2012) notes that surface waters in the western Arctic are generally more stratified now than in the past, but it is not clear whether there is any overall trend. In a transition to a more seasonal ice cover with a more pronounced seasonal freeze/melt cycle, one could expect to encounter hydrographical conditions in the IOBL similar

to the present dataset more frequently over larger regions than previously. Intermediary pycnoclines from wind-induced downward mixing of meltwater would thus be more common than before.

6. Conclusions

The present study presents one week of comprehensive measurements of underice turbulence, hydrography, currents, and ice drift. It investigates the processes governing ice–ocean exchange of heat and momentum for thin, late summer sea ice over a heavily stratified, shallow surface layer. Our study gives experimental evidence for the effects of such strong stratification on underice turbulence.

The observed discrepancy between turbulent and total ice–ocean stress is likely due to internal–inertial waves that are easily excited when the ocean is stratified all the way up to the surface (McPhee and Kantha 1989).

Ocean–ice heat flux is reduced because of two independent effects. The first effect is mechanical. When part of the downward momentum flux is carried by form drag or internal waves, the turbulent (Reynolds) ice–ocean stress is significantly smaller than the total ice–ocean stress. Internal wave and form drag contribute to the vertical transport of momentum, but not that of scalars such as heat or buoyancy. This has important implications for modeling when the turbulent friction velocity is approximated as the square root of the ice–ocean stress, which is not appropriate for the conditions analyzed in the present study. Using the square root of the kinematic turbulent stress as friction velocity, however, the bulk heat transfer coefficient is in good agreement with previous measurements. The second effect is thermodynamical. Likely, additional vertical salt or heat fluxes due to percolation through the ice matrix, or fresh, warm, buoyant meltwater that accumulates in leads and underice ponds, modify the heat and salt budget at the ice–ocean interface. This lowers the ice–ocean interface salinity and increases the interface temperature due to its freezing point condition and thereby reduces the heat fluxes. While our data support the existence of such effects, they are not directly proven. To find out how much of the salt flux is due to melt resulting from vertical oceanic mixing, and how much has to be due to other processes, one would need direct measurements of turbulent salt fluxes.

The proportions of the heat flux reductions discussed above warrant further investigation into their mechanism and how they behave for a wider range of ice–ocean stresses and stratification. In fact, both of these effects could act as negative feedback mechanisms. Increased ice melt leads to stronger stratification and thus

inhibits the vertical heat flux, and surface meltwater lowers the interface freezing point and thereby reduces ice–ocean heat fluxes. Thus, both effects reduce further melting.

We found that using the ice–ocean stress τ_w , as opposed to the turbulent Reynolds stress τ , Rossby similarity predicts the observed ice–ocean drag magnitude well. The present study confirms the theoretical findings of McPhee (2012) in that Rossby similarity can still predict the magnitude of the drag coefficient fairly well for a shallow pycnocline, but that the turning angle increases for larger friction velocities. However, it is important to note that even the shallow pycnocline case examined there is relatively conservative, with a well-mixed layer of roughly 20-m depth and a distinct pycnocline. We not only confirm this picture for a more extreme case of surface stratification, but also give a quick workaround [Eq. (19)] to adapt Rossby similarity to a new regime where it originally could not be applied. This yields acceptable turning angles for shallow pycnoclines while introducing a length scale d_p , roughly representative of the pycnocline depth, as the only additional parameter.

Acknowledgments. We thank Anders Sirevaag, Miles McPhee, Stephen Hudson, Cecilia Bitz, and Philipp Assmy for helpful discussions. In particular, Stephen Hudson provided the meteorology data from the weather mast and Agneta Fransson ice core salinity profiles. Two anonymous reviewers have provided valuable comments that helped to improve the paper. The help of the captain and crew of the R/V *Lance* and all participants of the ICE 2012 cruise is much appreciated, particularly that of Haakon Hop and his diving team. This study has been funded by the Centre for Ice, Climate and Ecosystems (ICE) at the Norwegian Polar Institute as part of the ICE Fluxes project.

REFERENCES

- Clarke, R., and G. Hess, 1974: Geostrophic departure and the functions A and B of Rossby-number similarity theory. *Bound.-Layer Meteor.*, **7**, 267–287, doi:10.1007/BF00240832.
- Cole, S., M. Timmermans, J. Toole, R. Krishfield, and F. Thwaites, 2014: Ekman veering, internal waves, and turbulence observed under Arctic sea ice. *J. Phys. Oceanogr.*, **44**, 1306–1328, doi:10.1175/JPO-D-12-0191.1.
- Comiso, J. C., 2012: Large decadal decline of the Arctic multiyear ice cover. *J. Climate*, **25**, 1176–1193, doi:10.1175/JCLI-D-11-00113.1.
- Du Vachat, R., and L. Musson-Genon, 1982: Rossby similarity and turbulent formulations. *Bound.-Layer Meteor.*, **23**, 47–68, doi:10.1007/BF00116111.
- Ekman, V. W., 1905: On the influence of the earth's rotation on ocean-currents. *Ark. Mat., Astron. Fys.*, **2**, 1–52.
- Fer, I., 2006: Scaling turbulent dissipation in an Arctic fjord. *Deep-Sea Res. II*, **53**, 77–95, doi:10.1016/j.dsr2.2006.01.003.
- Fofonoff, N. P., and R. C. Millard Jr., 1983: Algorithms for computation of fundamental properties of seawater. UNESCO Tech. Paper in Marine Science 44, 58 pp. [Available online at <http://unesdoc.unesco.org/images/0005/000598/059832eb.pdf>.]
- Grachev, A., C. Fairall, P. Persson, E. Andreas, and P. Guest, 2005: Stable boundary-layer scaling regimes: The SHEBA data. *Bound.-Layer Meteor.*, **116**, 201–235, doi:10.1007/s10546-004-2729-0.
- , E. Andreas, C. Fairall, P. Guest, and P. G. Persson, 2013: The critical Richardson number and limits of applicability of local similarity theory in the stable boundary layer. *Bound.-Layer Meteor.*, **147**, 51–82, doi:10.1007/s10546-012-9771-0.
- Hakkinen, S., A. Proshutinsky, and I. Ashik, 2008: Sea ice drift in the Arctic since the 1950s. *Geophys. Res. Lett.*, **35**, L19704, doi:10.1029/2008GL034791.
- Holland, M. M., 2003: An improved single-column model representation of ocean mixing associated with summertime leads: Results from a SHEBA case study. *J. Geophys. Res.*, **108**, 3107, doi:10.1029/2002JC001557.
- Hudson, S. R., M. A. Granskog, A. Sundfjord, A. Randelhoff, A. H. H. Renner, and D. V. Divine, 2013: Energy budget of first-year Arctic sea ice in advanced stages of melt. *Geophys. Res. Lett.*, **40**, 2679–2683, doi:10.1002/grl.50517.
- Kwok, R., G. Spreen, and S. Pang, 2013: Arctic sea ice circulation and drift speed: Decadal trends and ocean currents. *J. Geophys. Res.*, **118**, 2408–2425, doi:10.1002/jgrc.20191.
- Leppäranta, M., 2011: *The Drift of Sea Ice*. Springer, 347 pp., doi:10.1007/978-3-642-04683-4.
- Lu, P., Z. Li, B. Cheng, and M. Leppäranta, 2011: A parameterization of the ice–ocean drag coefficient. *J. Geophys. Res.*, **116**, C07019, doi:10.1029/2010JC006878.
- Maslanik, J. A., C. Fowler, J. Stroeve, S. Drobot, J. Zwally, D. Yi, and W. Emery, 2007: A younger, thinner Arctic ice cover: Increased potential for rapid, extensive sea-ice loss. *Geophys. Res. Lett.*, **34**, L24501, doi:10.1029/2007GL032043.
- McPhee, M. G., 1978: A simulation of inertial oscillation in drifting pack ice. *Dyn. Atmos. Oceans*, **2**, 107–122, doi:10.1016/0377-0265(78)90005-2.
- , 1979: The effect of the oceanic boundary layer on the mean drift of pack ice: Application of a simple model. *J. Phys. Oceanogr.*, **9**, 388–400, doi:10.1175/1520-0485(1979)009<0388:TEOTOB>2.0.CO;2.
- , 1981: An analytic similarity theory for the planetary boundary layer stabilized by surface buoyancy. *Bound.-Layer Meteor.*, **21**, 325–339, doi:10.1007/BF00119277.
- , 1982: Sea ice drag laws and simple boundary layer concepts, including application to rapid melting. U.S. Army Cold Regions Research and Engineering Laboratory Tech. Rep., 25 pp.
- , 1992: Turbulent heat flux in the upper ocean under sea ice. *J. Geophys. Res.*, **97**, 5365–5379, doi:10.1029/92JC00239.
- , 2008: *Air-Ice-Ocean Interaction: Turbulent Ocean Boundary Layer Exchange Processes*. Springer, 215 pp., doi:10.1007/978-0-387-78335-2.
- , 2012: Advances in understanding ice–ocean stress during and since AIDJEX. *Cold Reg. Sci. Technol.*, **76–77**, 24–36, doi:10.1016/j.coldregions.2011.05.001.
- , and L. H. Kantha, 1989: Generation of internal waves by sea ice. *J. Geophys. Res.*, **94**, 3287–3302, doi:10.1029/JC094iC03p03287.
- , G. A. Maykut, and J. H. Morison, 1987: Dynamics and thermodynamics of the ice/upper ocean system in the marginal ice zone of the Greenland Sea. *J. Geophys. Res.*, **92**, 7017–7031, doi:10.1029/JC092iC07p07017.

- Morison, J. H., and M. G. McPhee, 2001: Ice–ocean interaction. *Encyclopedia of Ocean Sciences*, Academic Press, 1271–1281, doi:[10.1006/rwos.2001.0003](https://doi.org/10.1006/rwos.2001.0003).
- , —, and G. A. Maykut, 1987: Boundary layer, upper ocean, and ice observations in the Greenland Sea marginal ice zone. *J. Geophys. Res.*, **92**, 6987–7011, doi:[10.1029/JC092iC07p06987](https://doi.org/10.1029/JC092iC07p06987).
- Notz, D., M. G. McPhee, M. G. Worster, G. A. Maykut, K. H. Schlünzen, and H. Eicken, 2003: Impact of underwater-ice evolution on Arctic summer sea ice. *J. Geophys. Res.*, **108**, 3223, doi:[10.1029/2001JC001173](https://doi.org/10.1029/2001JC001173).
- Olbers, D., J. Willebrand, and C. Eden, 2012: *Ocean Dynamics*. Springer, 708 pp., doi:[10.1007/978-3-642-23450-7](https://doi.org/10.1007/978-3-642-23450-7).
- Padman, L., and S. Erofeeva, 2004: A barotropic inverse tidal model for the Arctic Ocean. *Geophys. Res. Lett.*, **31**, L02303, doi:[10.1029/2003GL019003](https://doi.org/10.1029/2003GL019003).
- Prandke, H., and A. Stips, 1998: Test measurements with an operational microstructure-turbulence profiler: Detection limit of dissipation rates. *Aquat. Sci.*, **60**, 191–209, doi:[10.1007/s000270050036](https://doi.org/10.1007/s000270050036).
- Renner, A. H., S. Hendricks, S. Gerland, J. Beckers, C. Haas, and T. Krumpfen, 2013: Large-scale ice thickness distribution of first-year sea ice in spring and summer north of Svalbard. *Ann. Glaciol.*, **54**, 13–18, doi:[10.3189/2013AoG62A146](https://doi.org/10.3189/2013AoG62A146).
- Rosby, C.-G., and R. B. Montgomery, 1935: *The Layer of Frictional Influence in Wind and Ocean Currents*. Papers in Physical Oceanography and Meteorology, Vol. 3, Woods Hole Oceanographic Institute, 101 pp., doi:[10.1575/1912/1157](https://doi.org/10.1575/1912/1157).
- Sakshaug, E., 2004: Primary and secondary production in the Arctic seas. *The Organic Carbon Cycle in the Arctic Ocean*, R. Stein and R. MacDonald, Eds., Springer, 57–81, doi:[10.1007/978-3-642-18912-8_3](https://doi.org/10.1007/978-3-642-18912-8_3).
- Schmidt, G. A., C. M. Bitz, U. Mikolajewicz, and L.-B. Tremblay, 2004: Ice–ocean boundary conditions for coupled models. *Ocean Modell.*, **7**, 59–74, doi:[10.1016/S1463-5003\(03\)00030-1](https://doi.org/10.1016/S1463-5003(03)00030-1).
- Shaw, W. J., T. P. Stanton, M. G. McPhee, and T. Kikuchi, 2008: Estimates of surface roughness length in heterogeneous under-ice boundary layers. *J. Geophys. Res.*, **113**, C08030, doi:[10.1029/2007JC004550](https://doi.org/10.1029/2007JC004550).
- Sirevaag, A., 2009: Turbulent exchange coefficients for the ice/ocean interface in case of rapid melting. *Geophys. Res. Lett.*, **36**, L04606, doi:[10.1029/2008GL036587](https://doi.org/10.1029/2008GL036587).
- , M. G. McPhee, J. H. Morison, W. J. Shaw, and T. P. Stanton, 2010: Wintertime mixed layer measurements at Maud Rise, Weddell Sea. *J. Geophys. Res.*, **115**, C02009, doi:[10.1029/2008JC005141](https://doi.org/10.1029/2008JC005141).
- Skyllingstad, E. D., C. A. Paulson, W. S. Pegau, M. G. McPhee, and T. Stanton, 2003: Effects of keels on ice bottom turbulence exchange. *J. Geophys. Res.*, **108**, 3372, doi:[10.1029/2002JC001488](https://doi.org/10.1029/2002JC001488).
- Steele, M., J. H. Morison, and N. Untersteiner, 1989: The partition of air-ice-ocean momentum exchange as a function of ice concentration, floe size, and draft. *J. Geophys. Res.*, **94**, 12 739–12 750, doi:[10.1029/JC094iC09p12739](https://doi.org/10.1029/JC094iC09p12739).
- Timco, G., and R. Frederking, 1996: A review of sea ice density. *Cold Reg. Sci. Technol.*, **24**, 1–6, doi:[10.1016/0165-232X\(95\)00007-X](https://doi.org/10.1016/0165-232X(95)00007-X).
- Toole, J. M., M.-L. Timmermans, D. K. Perovich, R. A. Krishfield, A. Proshutinsky, and J. A. Richter-Menge, 2010: Influences of the ocean surface mixed layer and thermohaline stratification on Arctic sea ice in the central Canada basin. *J. Geophys. Res.*, **115**, C10018, doi:[10.1029/2009JC005660](https://doi.org/10.1029/2009JC005660).
- Untersteiner, N., 1968: Natural desalination and equilibrium salinity profile of perennial sea ice. *J. Geophys. Res.*, **73**, 1251–1257, doi:[10.1029/JB073i004p01251](https://doi.org/10.1029/JB073i004p01251).
- Wadhams, P., and N. Toberg, 2012: Changing characteristics of Arctic pressure ridges. *Polar Sci.*, **6**, 71–77, doi:[10.1016/j.polar.2012.03.002](https://doi.org/10.1016/j.polar.2012.03.002).
- Yamazaki, H., and T. Osborn, 1990: Dissipation estimates for stratified turbulence. *J. Geophys. Res.*, **95**, 9739–9744, doi:[10.1029/JC095iC06p09739](https://doi.org/10.1029/JC095iC06p09739).